Cellular Structures for Solid Fuel Grain Reinforcement: Mechanical and Combustion Performance in Conventional and Non-Conventional Hybrid Rocket Engines

By Christian Paravan[1,*], Riccardo Bisin[1], Anwer Hashish[1], Alberto Verga[1]

[1]Space Propulsion Laboratory, Politecnico di Milano, Milan, Italy

*christian.paravan@polimi.it

Reinforcement of the mechanical properties of liquefying fuel formulations based on paraffin waxes is typically pursued by blending with thermoplastic polymers. Such a strategy implies the reduction of the entrainment mass transfer due to the increased viscosity of the surface melt fuel layer. An alternative strategy for fuel grain mechanical properties enhancement is the use of 3D-printed polymeric structures embedded in the fuel grain. Open-cell structures as the gyroid feature suitable characteristics for this task: (i) open-cell structure hosting the thermoplastic fuel, (ii) uniformity, (iii) efficiency of volume usage, and (iv) prototyping promptness. In the first part of the work, the use of fuel blends based on styrene-ethylene-butylene-styrene grafted with maleic anhydride (SEBS) is contrasted with the effects of embedding cellular structures for the reinforcement of the mechanical properties of paraffin-based fuel grains. Then, the combustion behaviour of a vortex flow pancake (VFP) engine burning liquefying fuel formulations without/with reinforcing structures is investigated by a series of experiments showing how this peculiar implementation together with the mechanical-ballistic properties of reinforced fuels can help with the full exploitation of paraffin-based compositions for in-space propulsion.

Key Words: Paraffin-based fuel, Cellular structure, Mechanical properties, Regression rate, Vortex flow pancake

Nomenclature

L/D	:	burning area, m^2
ABS	:	acrylonitrile-butadiene-styrene
c^*	:	characteristic velocity, m/s
D	:	grain port diameter, m
D_t	:	throat diameter, m
DSC	:	differential scanning calorimetry
E	:	Young modulus (cellular structure), MPa
E_{bulk}	:	Young modulus of the bulk material, MPa
G	:	propellant mass flux, $\text{kg}/(\text{s m}^2)$
G_f	:	fuel mass flux, $\text{kg}/(\text{s m}^2)$
G_{ox}	:	oxidizer mass flux, $\text{kg}/(\text{s m}^2)$
H_c	:	combustion chamber height, m
HRE	:	hybrid rocket engine
L/D	:	length-to-diameter ratio, -
L_{Grain}	:	solid fuel grain length, mm
$\dot{m}$	:	propellant mass flow rate, kg/s
$\dot{m}_f$	:	fuel mass flow rate, kg/s
$\dot{m}_{ox}$	:	oxidizer mass flow rate, kg/s
$m_{N2,in,}$	:	initial mass of the N_2-side disk, kg
$m_{N2,fin}$	:	final mass of the N_2-side disk, kg
$m_{Noz,in,}$	:	initial mass of the nozzle disk, kg
$m_{Noz,fin}$	:	final mass of the nozzle-side disk, kg
O/F	:	oxidizer-to-fuel ratio (mass), -
p_c	:	combustion chamber pressure, MPa
PLA	:	poly-lactic acid
R	:	VFP combustion chamber radius, m
r_f	:	regression rate, mm/s
SEBS	:	styrene-ethylene-butylene-styrene copolymer grafted with maleic anhydride
SHRE	:	SPLab HRE (lab-scale engine)
SVFP	:	SPLab VFP (lab-scale engine)
T	:	temperature, K

$T_{on.melt}$	:	melting onset temperature, K
$T_{on.dea}$	:	degradation onset temperature, K
$T_{end.dea}$	:	degradation end temperature, K
t	:	time, s
TG	:	thermogravimetry
TMD	:	theoretical maximum density, kg/m^3
VFP	:	vortex flow pancake
Δm	:	mass change (burning tests), kg
$\Delta m_{\%}$	:	percent mass change (TG tests), %
Δt	:	time interval, s
Δt_b	:	burning time, s
ε	:	elongation, %
η_{c*}	:	c^* combustion efficiency, %
ρ	:	material density (cellular structure), kg/m^3
$\tilde{\rho}$	:	relative density (cellular structure), -
$\tilde{\rho}_{\%}$	:	percent relative density (cellular structure), %

1. Introduction

Slow fuel r_f and low combustion efficiency are typically taken as the main factors hampering HRE development.[1] Liquefying fuels offer attractive r_f performance with possible breakthrough effects on the use of hybrid rocket propulsion in large thrust systems (i.e., small- and medium-size launchers with reduced environmental impact and operating costs). [2,3] The relative ease of handling of thermoplastic liquefying fuels as paraffin-based compositions, provides safe ground operations and enables recurring costs reduction for launch and in-space applications. On the other hand, the use of paraffin-based fuel formulations is limited by (i) the relatively poor mechanical properties of waxes,[4,5] and (ii) the impact of liquefying fuels on the combustion efficiency of the hybrid engine. [6]

Blending of solid paraffin wax with a reinforcing thermoplastic polymer is a suitable strategy for mechanical properties enhancement.[4),5),7),8)] The frail and brittle behaviour of the paraffin wax is mitigated by the reinforcing material providing improved elasticity and deformability. Yet, the high viscosity of the reinforcing polymers hinders the entrainment mass transfer providing fast r_f to the paraffin-based fuel.[4),5),9),10)] The Space Propulsion Laboratory (SPLab) of Politecnico di Milano is active in the research field of new fuel formulations for hybrid propulsion and, while working on conventional grain reinforcing methods, has recently proposed an innovative strategy for paraffin-based fuel grain mechanical response enhancement:[7),11)] 3D-printed cellular structures have been embedded in the fuel matrix to improve the mechanical response of the fuel grain. The cellular structure sustains loads and stresses, thus limiting the reinforcing polymer mass fraction in the paraffin-based fuel: consequently, the melt fuel viscosity can be tailored to provide entrainment mass transfer and fast r_f. Fuel grains whose mechanical properties are reinforced by structures embedded in the solid fuel grains are called *armored grains.* [7)]

Combustion efficiency enhancement can be pursued by intense fuel/oxidizer vapors mixing. The vortex flow pancake (VFP) is a non-conventional engine configuration offering compact design and promoting high combustion efficiency by the internal flow-field. [12)-16)] The engine compactness and the peculiar L/D (typically < 1) suggest the easy fit of the VFP to several platforms for in-space missions. In this respect, the synergy of the VFP configuration with thermoplastic fuels is an interesting opportunity for the realization of low-cost propulsion systems: though for in-space propulsion large thrust levels are not a driver, tailorable r_f and safe and easy manufacturing are key points for efficient design (recurring cost reduction, safe operations).

This work discusses recent results on the development of liquefying fuel formulations obtained at SPLab. Both conventional and non-conventional HRE configurations are investigated at lab-scale. In the first part of the work, the use of fuel blends based on SEBS is contrasted with the effects of embedding cellular structures for the reinforcement of the mechanical properties of paraffin-based fuel grains. The affordability of fast enough r_f in combination with suitable mechanical properties is the driver of the investigation. Then, the combustion behaviour of a VFP engine burning liquefying fuel formulations without/with reinforcing structures is investigated by a series of experiments showing how this peculiar implementation together with the mechanical-ballistic properties of reinforced fuels can help with the full exploitation of the features of paraffin-based compositions.

The work is presented providing a short background on cellular structures (Sec. 2), an introduction of the materials and methods considered in the analysis (Sec. 3), and an analysis of the mechanical and burning performance of blends and structure-reinforced grains (Sec. 4). Conclusions of the work and recommendations for future developments will be given in Sec. 5.

2. Cellular Structures: A Short Background

A structure composed by structs delimiting randomly/periodically repeating closed/open cells is called a cellular structure.[17)] This class of structures (also known as cellular solids, or lattice materials) include, for example, foams and honeycombs. Additive manufacturing, and, in particular, fuse deposition method, well suit to the production of cellular structures. The mechanical response of a cellular structure depends on different factors: (i) the properties of the material the lattice is created from, (ii) the structure topology and the shape of the cell edges, and (iii) the relative density $\tilde{\rho}$, defined as the ratio between the density of the lattice ρ (i.e., the lattice structure mass divided by the enveloped volume) and the density of the solid material, TMD. When considering the use as reinforcing structures for solid fuel grains, open cell structures feature an empty volume easily filled by melted paraffin during casting.

The gyroid is a triply periodic, open-cell structure featuring a minimal surface for a given volume. [18)] Figure 1 shows a representation of the unit cell of a gyroid, while Figure 2 reports some 3D-printed structures (30 mm diameter, 50 mm height) [7)] with different infills (i.e., $\tilde{\rho} = \rho/TMD$).
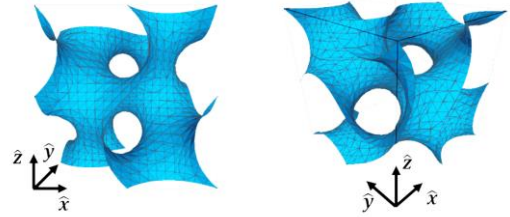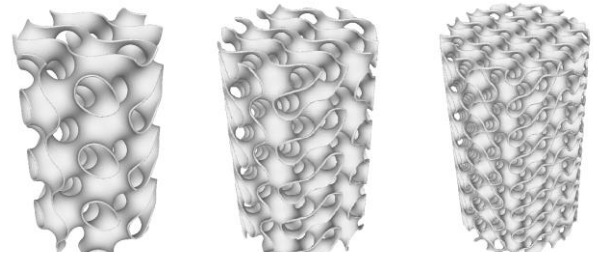

Figure 1. Gyroid unit cell.

Figure 2. Gyroid structures with (a) 7%, (b) 10%, and (c) 15% infill.

Gyroid mechanical properties are strongly related to $\tilde{\rho}$ and the following trends are identified for the Young modulus [Eqs. (1-2)] and the yield stress [Eq. (3)]:

$$E/E_{bulk} \propto \tilde{\rho}^2 \qquad (1)$$
$$E/E_{bulk} \propto \tilde{\rho} \qquad (2)$$
$$\sigma/E_{bulk} \propto \tilde{\rho}^2 \qquad (3)$$

With Eq. (1) holding for bending-dominated structures (i.e., structures respond to applied loads by the bending deformation of the struts composing the cell.), Eq. (2) that is valid for stretch-dominated structures (i.e., structures in which the cell edges stretch

because of the applied loads), and Eq. (3) that has a general validity. Further details on cellular structures and their early characterization as reinforcing elements in solid fuel grains are reported in Refs. 7)-11). A critical comparison between different 3D-printed structures is reported in Ref. 11). From the latter analysis, the gyroid emerges as a suitable candidate from the mechanical and ballistic point of view.

3. Materials and Methods

Ingredients and tested fuel formulations are introduced first, before passing to a description of the implemented analysis methods. The latter include pre-burning analyses (DSC-TG, rheology, mechanical compression) and burning behavior investigations.

3.1. Fuel Formulations

3.1.1. Fuel Grain Ingredients

In the analysis, a commercial microcrystalline wax, SASOL 0907 (produced by SASOLWax Gmbh, Germany), is extensively characterized (and is hereinafter labeled simply as 0907). The reinforcing polymer is SEBS (Merck KgaA, Germany).

Tested formulations include pure paraffin (with 1 wt% C as opacifier), and wax-SEBS blends. The latter are tested with microcrystalline wax and include: a blend of 95 wt% SASOL 0907 and 5 wt% SEBS, and a composition with 90 wt% of paraffin and 10 wt% styrenic polymer (see Table **1**).

Table 1. Tested fuel formulations. *Printed with special algorithms.

Fuel	Details
SF-01	0907 (99 wt%) + C (1 wt%)
SF-02	0907 (94 wt%) + SEBS (5 wt%)+ C (1 wt%)
SF-03	0907 (89 wt%) + SEBS (10 wt%) + C(1 wt%)
SF-01-ABS-i10	SF-01 embedding ABS gyroid ($\tilde{\rho} = 10\%$)
SF-01-ABS-i15	SF-01 embedding ABS gyroid ($\tilde{\rho} = 15\%$)
SF-02-ABS-i10	SF-02 embedding ABS gyroid ($\tilde{\rho} = 10\%$)
SF-02-ABS-i15s	SF-02 embedding ABS gyroid ($\tilde{\rho} = 15\%$)*
SF-03-ABS-i15s	SF-03 embedding ABS gyroid ($\tilde{\rho} = 15\%$)*

3.1.2. 3D-printed Structures: Materials & Structures

The thermoplastic polymer considered in the analysis is ABS, considering its overall thermal and mechanical properties. Differently from other polymers (e.g., PLA), ABS show no glass transition issues at the casting temperatures typical of SF-01 or SEBS-MA-based blends. Filaments are provided by PRUSA (Czech Republic).

The only reinforcing structure considered in the study is the gyroid. This element is printed with different infills ($\tilde{\rho}_{\%} = 10\%$ and $\tilde{\rho}_{\%} = 15\%$) and by different algorithms. In particular, the different printing algorithms aims at providing variations of the infill value to minimize differences in the infill of the actual structures (see, for further discussions, Ref. 11). Due to this,

ABS-15s is not considered in the mechanical characterization part (non-optimized printing process). Table 1 and Table 2 include details on the printed structures as embedded in the fuel grains and di per se.

Table 2. Tested gyroid structures. ABS-i15s is produced with a modified method, thus it is not considered for mechanical characterization analyses.

Structure	Details
ABS-i10	ABS gyroid ($\tilde{\rho} = 10\%$), standard method
ABS-i15	ABS gyroid ($\tilde{\rho} = 15\%$), standard method
ABS-i15s	ABS gyroid ($\tilde{\rho} = 15\%$), modified method (cell length 8.25 mm)

3.1.3. Tested Fuels and Experimental Matrix Definition

A list of the tested fuel formulations (including blends and armored grains) is reported in Table **1**.

The experimental matrix is defined to provide a full characterization starting materials, of the structures (impact of the gyroid infill, of the printing materials, and of the printing process), and of the blends/armored grains.

In the pre-burning characterization:
- simultaneous DSC-TG is used to define the thermal behavior of the starting microcrystalline wax, of the 0907 + SEBS blends (SF-02 and SF-03), and of the printing polymers (ABS);
- rheological analyses are performed on the starting microcrystalline wax, and on the blends, to assess the impact of the reinforcing polymer on the melt layer viscosity under reference conditions;
- compression tests are performed on the printed structures and on solid fuel grains (blends and armored) to evaluate the printing material effect on the gyroid response as well as the mechanical response of the armored grains with respect to the blends.

In the burning analysis:
- formulations are tested in a conventional HRE configuration for r_f evaluation (relative grading);
- selected fuels are tested in the VFP engine to evaluate the ballistic response and combustion efficiency of liquefying fuels in a non-conventional engine geometry.

3.2. Experimental Setups
Experimental setups and conditions used for the pre-burning and burning characterizations are hereby reported.

3.2.1 Pre-burning Analyses
Simultaneous DSC-TG are performed in Ar (75 ml/min), with heating rate of 10 K/min at 0.1 MPa in a Netzsch STA 449 F5 Jupiter. The investigated temperature range spans from 298 K to 1273 K, while the specimen mas is 10 ± 0.5 mg. Relevant data are typically evaluated by the TG traces, with exception of the identification of the melting peak of the materials (if any). The tangent method is used for the definition of onset/end temperatures.

Rheological behavior of the starting wax and of the blends is evaluated by a TA AR2000Ex rheometer operating at 423 K, with shear rate in the range 10 to 1000 s^{-1}. Average data are presented with uncertainties given by standard deviation (over ≥ 2 runs).

Compression analyses are performed by MTS 810 universal testing machine. The hardware is displacement controlled. Compression tests are taken with crossbar speed of 1 mm/min, at the temperature of 295 ± 3 K. At least three tests are performed per each formulation. Data reduction is performed considering the indications of the ISO 604.[19] Single tests are used for the determination of relevant parameters (E, $\varepsilon_{Yield}, \sigma_{yield}, \varepsilon_{Break}, \sigma_{break}$), while, in the plots, ensemble average curves are reported (with error bars representing the standard deviation from the average value).

3.2.2 Burning Analysis: Lab-scale Engines

Combustion behavior of the tested fuels is evaluated by firings in lab-scale engines with conventional and non-conventional configurations. In both cases, the oxidizer is gaseous oxygen, differences being related to the combustion chamber configuration. The two facilities share the same control hardware, based on LabView, and implemented by a National Instruments Quad Core PXIe-8861 Controller. Oxidizer mass flow rate is controlled by a digital flowmeter providing live control of $\dot{m}_{ox}$ (quasi-steady burning, with no throttling). The SPLab HRE (SHRE) is a small motor with swirled oxidizer injection (geometrical swirl number at the injection section is 3.3), that is purposely designed to grant optical access to the head-end section of the burning sample (see Figure 3 and 4). Combustion chamber pressure is monitored by piezoresistive pressure transducers, and the signal is sampled at frequencies ≥ 3 kHz. High-speed acquisition of the burning is performed by Phantom V710 operating at ≥ 250 fps.

The SPLab VFP (SVFP) is designed based on the original engine configuration proposed in Ref. 12). A schematic view of the setup, highlighting the L/D < 1 is given in Figure 4. The system is described in detail in Refs. 13)-16).
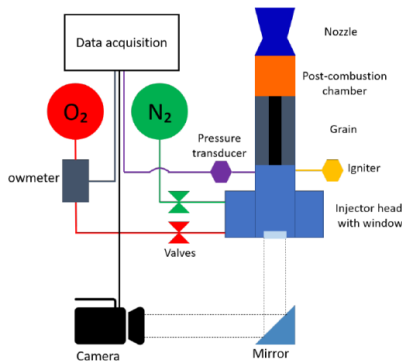
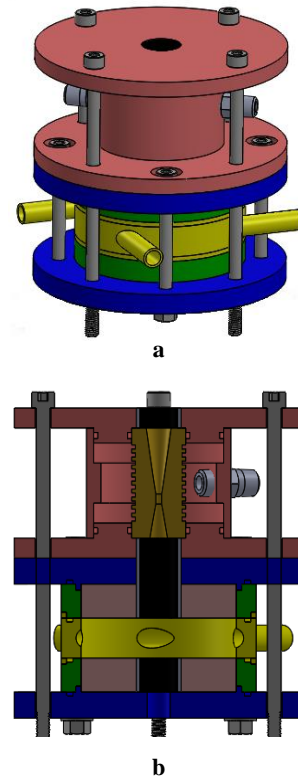

Figure 3. SPLab HRE engine: schematics.

Figure 4. SPLab VFP engine: (a) side view and (b) cross sectional view. Side view: injection ring is highlighted (yellow), water-cooled nozzle (pink). Cross sectional view: fuel grains sandwiching the injection ring are visible (light purple).

3.3. Data Reduction

Regression rate data reduction is based on thickness over time methods for both SHRE and SVFP. Combustion is started by a pyrotechnic primer charge whose burning products ignite the solid fuel grain. Combustion is quenched by nitrogen purge. Chamber pressure history in time is recorded and enables the definition of the burning time (Δt_b). In SHRE tests, $p_c(t)$ and video recording are synchronized. Ignition time is defined as the moment combustion chamber pressure rise is triggered by primer charge ignition.

For the both SHRE and SVFP, the r_f determination is based on mass-based thickness over time. For the conventional geometry engine relevant parameters of interest are evaluated as:

$$r_{f,ave}(\Delta t_b) = \frac{\Delta m}{TMD \cdot A_{b,ave} \cdot \Delta t_b} = \qquad (4)$$
$$= \frac{2\Delta m}{TMD \cdot \pi[D(t + \Delta t) + D(t)] \ L_{Grain} \cdot \Delta t_b}$$

$$G_{ox,ave}(\Delta t_b) = \frac{16 \, \dot{m}_{ox}}{\pi[D(t + \Delta t) + D(t)]^2} \qquad (5)$$

In the SVFP, the thickness over time method is based on the fuel grain mass consumption during the burning:

$$r_{f,ave}(\Delta t_b) = \frac{\Delta m}{TMD \cdot 2A_b \cdot \Delta t_b} =$$
$$= \frac{(m_{N2,in} - m_{N2,fin}) + (m_{Noz,in} - m_{Noz,fin})}{TMD \cdot 2A_b \cdot \Delta t_b} \qquad (6)$$

The value from the mass balance of the Eq. (6) is directly compared with the H_c variation during the test, which is directly measured. Thus, the oxidizer mass flux can be defined as:

$$G_{ox,ave}(\Delta t_b) = \frac{2\dot{m}_{ox}}{R[H_c(t + \Delta t_b) + H_c(t)]} \qquad (7)$$

For the SVFP, combustion efficiency is evaluated based on the c^* definition. The theoretical c^* from the test (c^*_{Ideal}) is evaluated based on its definition as derived by the firing data. The c^*_{Ideal} is calculated by the NASA CEA code, considering shifting equilibrium conditions. The achieved value is then compared to its experimental counterpart (c^*_{Real}). The latter is evaluated by the measured propellant mass flow rate [see Eq. (8)] and by the (measured) D_t. The combustion efficiency achieved by the SVFP during the run is then evaluated as

$$\eta_{c*} = \frac{c^*_{Real}}{c^*_{Ideal}} \qquad (8)$$

4. Results and Discussion

Results for the pre-burning and burning tests are hereby discussed. Pre-burning is presented first, then SHRE and SVFP data are introduced.

4.1. Pre-burning Characterization

Results from the DSC-TG analyses on SF-01, SF-02 and SF-03 are shown in Figure 5 and in Table 3.

Both SEBS-MA and ABS show no melting endotherm in the DSC traces, due to their amorphous nature. For microcrystalline wax-containing blends, the melting peak of the 0907 is always recognizable, and is not significantly shifted by the blending that creates a heterogeneous mix of wax and styrene-based polymer. Addition of SEBS-MA to the wax increase the degradation onset off the blend, thanks to the marked thermal resistance of the polymer (see Table 3).

Data on the rheological behavior of the microcrystalline wax and of the blends are reported in Table 4. Under the investigated conditions: (i) all the tested materials feature a Newtonian behavior, (ii) viscosity of the wax is altered by the SEBS-MA addition, with a significant increase for a polymer load of 10 wt% (i.e., + 600%).
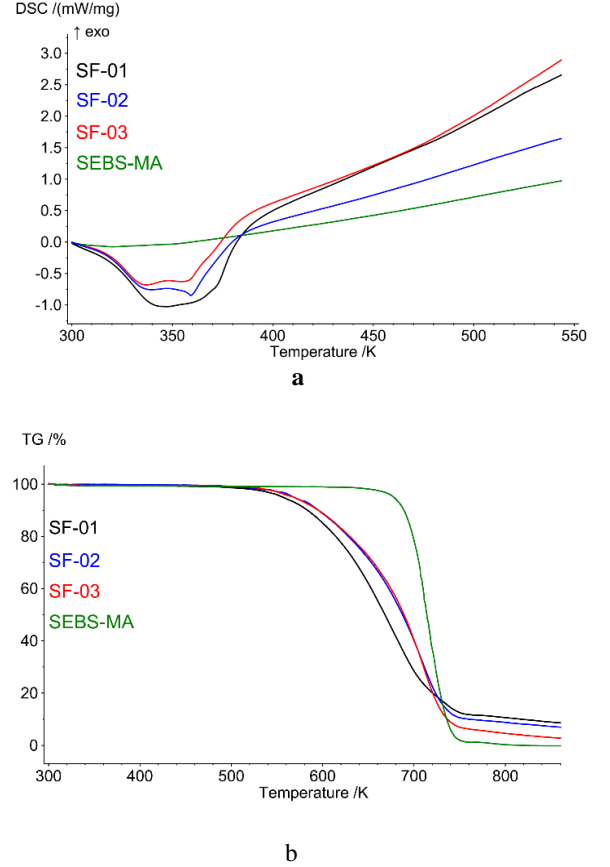
Figure 5. Thermal analysis traces for microcrystalline wax and blends with SEBS (10 K/min, Ar, 0.1 MPa): (a) DSC, (b) TG.

Table 3. DSC-TG data for the tested fuel formulations and for the printing/reinforcing polymers.

Fuel	$T_{on,melt}$ K	$T_{on,deg}$, K	$T_{end,deg}$, K	Δm ($873\ K \leq T \leq 303\ K$), %
SF-01	320	599	722	-91
SF-02	319	635	734	-93
SF-03	319	645	734	-97
SEBS	-	692	735	>-99
ABS	-	696	745	-99

Table 4. Rheological behavior of the tested fuel formulations (423 K, 1000 s^{-1}). Uncertainty by standard deviation over 2 tests.

Fuel Id.	η, Pa s
SF-01	0.006 ± 0.001
SF-02	0.014 ± 0.001
SF-03	$0.040 \pm$ N.Av.

Mechanical response to the compression tests is reported in Table 5 and Figure 6.

Table 5. Compression test results (1 mm/min, 296 ± 3 K). ABS-i15s and its armored grains are not considered due to the modified, non-optimal printing procedure.

Fuel Id.	E, MPa	ε_{Yield}, %	σ_{Yield}, MPa
SF-01	407 ± 18	1.47 ± 0.05	3.46 ± 0.13
SF-02	519 ± 30	1.34 ± 0.15	4.46 ± 0.15
SF-03	510 ± 15	1.86 ± 0.05	4.92 ± 0.29
ABS-i10	15 ± 1	6.59 ± 0.60	0.46 ± 0.03
ABS-i15	49 ± 1	5.11 ± 0.35	1.58 ± 0.03
SF-01-ABS-i15	327 ± 36	4.61 ± 0.38	3.52 ± 0.03
SF-02-ABS-i10	328 ± 33	1.58 ± 0.06	3.27 ± 0.14

4.2 Burning Behavior

Data for the relative ballistic grading of the tested fuel formulations are reported in Table 6 and Table 7. The presented data show $r_{f,ave}(G_{ox,ave})$ for at least three test per formulation, except where otherwise stated. Discussion of the results is performed considering SF-01 as baseline and contrasting the effects of the reinforcing structure on the ballistic response of similar fuel formulations. Minor differences exist on the $G_{ox,ave}$ data of the tested formulations, yet a comparison between the achieved data is possible.

Table 6. Relative ballistic grading of fuel formulations tested by the SHRE (gaseous O_2).

Fuel Id.	$G_{ox,ave}$, $kg/(m^2 s)$	$r_{f,ave}$, mm/s
SF-01	42 ± 2	1.31 ± 0.05
SF-02	44 ± 4	1.02 ± 0.05
SF-03	48 ± 2	0.88 ± 0.05
ABS	50 ± 11	0.54 ± 0.03
SF-01-ABS-i10	37 ± 3	2.21 ± 0.28
SF-01-ABS-i15	38 ± 1	1.91 ± 0.07
SF-01-ABS-i15s	42 ± 1	1.84 ± 0.09
SF-02-ABS-i10	32 ± 3	1.70 ± 0.15
SF-02-ABS-i15s	37 ± 1	1.57 ± 0.04
SF-03-ABS-i15s	45 ± 2	1.24 ± 0.04

Table 7. Relative ballistic grading of fuel formulations tested on the SVFP (gaseous O_2). * Single test data.

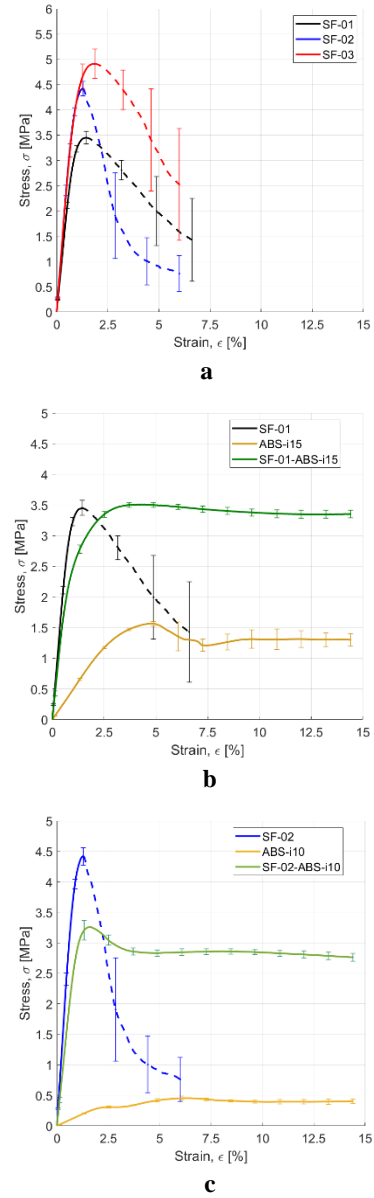| Fuel Id.	$G_{ox,ave}$, $kg/(m^2 s)$	$r_{f,ave}$, mm/s
SF-01*	8.8	0.82
SF-02	7.3 ± 0.0(3)	0.57 ± 0.02
SF-03	8.8 ± 0.1	0.48 ± 0.03
ABS	8.1 ± 0.0(1)	0.23 ± 0.03
SF-02-ABS-i10*	8.6	0.60

a

b

c

Figure 6. Compression behavior (ensemble curves, 1 mm/min, 296 ± 3 K): (a) wax and paraffin-SEBS-MA blends, (b)-(c) armored grains (SF-01-ABS-i15 and SF-02-ABS-i10) with the corresponding paraffin matrixes (SF-01 and SF-02) and embedded ABS gyroid structures (ABS-i15 and ABS-i10). Error bars are identified by standard deviation.

4.3 Discussion

The compression tests campaign at compression show that the SEBS-MA enhances both the stiffness (E) and the strength (σ_{Yield}) of the pristine SF-01 wax. In particular, the maximum stress is raised by 29% and 42% (refer to Table 5) when 5% and 10% of SEBS-MA are added to the SF-01, respectively. However, the SEBS-MA doped fuels still exhibit brittle behaviors, as suggested by the sudden drop after the σ_{Yield} in the $\sigma(\varepsilon)$ curves in Figure 6a. Hence, no plastic deformation is present, and the yield point coincides with the failure point. The widening of the error bars after the failure point (dashed regions

of the curves in Figure 6a) confirms the onset and propagation of cracks. Focusing on the mechanical behavior of armored grains in Figures 6b and 6c, these fuels are characterized by a plastic region after the σ_{Yield}, with a plateau stress around the 3.4 and 2.9 MPa for the SF-01-ABS-i15 and the SF-02-ABS-i10, respectively. The insertion of 3D printed ABS gyroid structures in the fuel formulation overcome the intrinsic brittleness of both the pure microcrystalline wax (SF-01) and its blend with 5% SEBS-MA (i.e., the SF-02 sample). Hence, the armored grains are characterized by greater toughness than the paraffin fuels, and the former can absorb higher strain energy than the latter. Indeed, the structural response of armored grains is affected by the mechanical behavior of the two components: the paraffin matrix and the ABS structures. The SF-01-ABS-i15 is based on the less stiff and less strong paraffin wax (the SF-01) and on the most performing gyroid (ABS-i15). On the contrary, the SF-02-ABS-i10 features the paraffin wax with higher mechanical properties than the SF-01, but the ABS-i10, which has significantly lower E and σ_{Yield} than the ABS-i15. As a result, the SF-01-ABS-i15 and the SF-02-ABS-i10 show comparable stiffnesses, strengths and curves $\sigma(\varepsilon)$.

Considering the SHRE ballistic data, despite minor differences on the $G_{ox,ave}$ values, the achieved results show the effects of melt layer viscosity and reinforcing structure on the burning behavior of the formulations. Under the investigated conditions the melt fuel viscosity increase due to the SEBS blending promotes a $r_{f,ave}$ decrease of 22% and 33% for SF-02 and SF-03, respectively. Under the investigated conditions, all the tested paraffin-based formulations show a higher $r_{f,ave}$ than the ABS (see Table 6). The SF-01-ABS-fuels exhibit faster regression rates than SF-01, with percent increases over the baseline from 69% (SF-01-ABS-i10) to 46% and 40% for the grains reinforced with the 15%-infill gyroid. SF-01-ABS-i15 and SF-01-ABS-i15s data show, indeed, partially overlapped error bars (Table 6). Such a performance reduction with the increase in the infill gyroid is likely related to the higher mass of the reinforcing structure.
SF-02-ABS-i10 shows a regression rate enhancement of 67% with respect to the non-armored counterpart. Despite the $G_{ox,ave}$ difference between SF-02 and SF-02-ABS-i10, the result in in good agreement with the performance difference between SF-01 and SF-01-ABS-i10.
The reinforcing structure effect on the SF-03 ballistic response is similar to that of the SF-01, with a 40% $r_{f,ave}$ increase of SF-03-ABS-i15s over SF-03.

The SVFP data of Table 7 show trends for the paraffin-based blends with $r_{f,ave}$ reduction of 30% between SF-01 and SF-02, and of 40% between the baseline and the fuel with a 10 wt% load of SEBS. Under the investigated conditions, SF-01 show a regression rate performance with a 72% increase with respect to ABS. When comparing the SF-02 data with those of the SF-02-ABS-i10, differently from the SHRE case, no marked effects on the ballistic response are noted. For these two fuel formulations the $r_{f,ave}$ data are nearly overlapped when considering the data scattering (see Table 7).

Under the investigated conditions, SF-01 exhibits η_{c*} = 90% (datum referring to a single firing), while, for SF-02 and SF-03, values of 97 ± 1% and 98 ± 1% were achieved. The two ABS firings performed show η_{c*} = 98 ± 1%. Thus, under the investigated conditions, the intensity of the vortex flow seems highly effective in promoting high c* combustion efficiency for formulations with reduced (or absent) entrainment mass fraction. The achieved results are particularly interesting when considering that the SVFP does not feature a dedicated post-combustion chamber. The combustion mechanism of SF-01 (regression due to vaporization and entrainment mass transfer) and the mechanical properties of the fuel are likely playing a crucial role in the combustion efficiency of the system, in spite of the vortex mixing (i.e., detachment of fuel slivers). Yet, further tests are required, in particular, for the pure paraffin fuel, to achieve a more consolidated result.

The mechanical and ballistic results attest that the reinforcement of paraffin waxes via SEBS-MA blending approach can be achieved at the expense of regression rate reduction improvement. Hence, a trade-off between mechanical and ballistic performance is unavoidable when dealing with paraffin blend. On the contrary, the insertion of purposely 3D printed gyroid structures in the paraffin fuel (i.e., the armored grains) provides the paraffin itself with a plastic behavior without lowering the regression rate. The mechanical and ballistic properties of armored grains can be tailored by changing the paraffin fuel formulation and the infill fraction for the gyroid.

5. Conclusions and Future Developments
The work discusses strategies for paraffin-based fuel reinforcement. The conventional wax blending with reinforcing polymers is contrasted with the armored grain concept. In the latter, a scaffold structure is embedded in the fuel grain to enhance its mechanical properties. The two approaches are then combined in an effort toward the identification of a formulation with suitable characteristics from the mechanical and ballistic point of view. The gyroid, a triply periodic minimum surface structure, is considered as reinforcing structure. Gyroids are produced by 3D-printing, using ABS as printing material. The ballistic response of the investigated fuels is evaluated at lab-scale in HREs with conventional and non-conventional configurations. The former is an engine burning cylindrical grains with single, circular, central port perforation. The latter is a VFP engine. Experimental results from pre-burning and conventional HRE combustion tests show how the use of a scaffold structure provides a combination of relatively high mechanical properties with fast regression rates, while the simple blending technique produces grain structural improvements at the expenses of the entrainment mass transfer (due to the melt layer viscosity increase). Under the investigated conditions, the reinforcing structure impact on the ballistic response of the VFP appears more limited. This is probably due to the impact of the vortex combustion process promoting more intense propellant mixing also in the absence of the 3D-printed inserts (whose structure promotes an uneven regressing surface

profile). The so far achieved results require further investigations, in particular, for the VFP case. Further developments of the work include the study of different paraffin waxes as embedding materials for the reinforcing structures (to further investigate the structure impact on thermal and mechanical properties of the grains), and the evaluation of the armored grain concept at larger grain scales.

References

1) D. Altman, A. Holzman, Overview and History of Hybrid Rocket Propulsion, in: Fundamentals of Hybrid Rocket Combustion and Propulsion, American Institute of Aeronautics and Astronautics, 2007: pp. 1–36. https://doi.org/10.2514/5.9781600866876.0001.0036.

2) M.A. Karabeyoglu, D. Altman, B.J. Cantwell, Combustion of Liquefying Hybrid Propellants: Part 1, General Theory, Journal of Propulsion and Power. 18 (2002) 610–620. https://doi.org/10.2514/2.5975.

3) M.A. Karabeyoglu, B.J. Cantwell, Combustion of Liquefying Hybrid Propellants: Part 2, Stability of Liquid Films, Journal of Propulsion and Power. 18 (2002) 621–630. https://doi.org/10.2514/2.5976.

4) C. Paravan, L. Galfetti, F. Maggi, A Critical Analysis of Paraffin-based Fuel Formulations for Hybrid Rocket Propulsion, in: 53rd AIAA/SAE/ASEE Joint Propulsion Conference, American Institute of Aeronautics and Astronautics, 2017. https://doi.org/10.2514/6.2017-4830.

5) Y. Tang, S. Chen, W. Zhang, R. Shen, L.T. DeLuca, Y. Ye, Mechanical Modifications of Paraffin-based Fuels and the Effects on Combustion Performance, Propellants, Explosives, Pyrotechnics. 42 (2017) 1268–1277. https://doi.org/10.1002/prep.201700136.

6) C. Carmicino, F. Scaramuzzino, A. Russo Sorge, Trade-off between paraffin-based and aluminium-loaded HTPB fuels to improve performance of hybrid rocket fed with N2O, Aerospace Science and Technology. 37 (2014) 81–92. https://doi.org/10.1016/j.ast.2014.05.010.

7) R. Bisin, C. Paravan, S. Alberti, L. Galfetti, A new strategy for the reinforcement of paraffin-based fuels based on cellular structures: The armored grain — Mechanical characterization, Acta Astronautica. 176 (2020) 494–509. https://doi.org/10.1016/j.actaastro.2020.07.003.

8) T. Ishigaki, I. Nakagawa, Improving Physical Properties of Wax-Based Fuels and Its Effect on Regression Rate, Journal of Propulsion and Power. 36 (2020) 123–128. https://doi.org/10.2514/1.B37613.

9) M. Kobald, C. Schmierer, H.K. Ciezki, S. Schlechtriem, E. Toson, L.T. De Luca, Viscosity and Regression Rate of Liquefying Hybrid Rocket Fuels, Journal of Propulsion and Power. 33 (2017) 1245–1251. https://doi.org/10.2514/1.B36207.

10) K. Bilge, U. Kokal, N.B. Emerce, U.C. Yildiz, M. Baysal, A. Karabeyoglu, Selection Criteria for Tackifier Addition to Paraffin Wax based Hybrid Rocket Fuels, in: AIAA Propulsion and Energy 2019 Forum, American Institute of Aeronautics and Astronautics, 2019. https://doi.org/10.2514/6.2019-3921.

11) R. Bisin, C. Paravan, S. Parolini, L. Galfetti, Impact of 3D-printing on the Mechanical Reinforcement and the Ballistic Response of Paraffin-based Fuels: The Armored Grain, in: AIAA Propulsion and Energy 2020 Forum, American Institute of Aeronautics and Astronautics, 2020. https://doi.org/10.2514/6.2020-3735.

12) D.M. Gibbon, G.S. Haag, Investigation of an Alternative Geometry Hybrid Rocket for Small Spacecraft Orbit Transfer, Surrey Satellite Technology LTD, Guilford, UK, 2001. https://apps.dtic.mil/sti/citations/ADA393398 (accessed December 6, 2021).

13) C. Paravan, J. Glowacki, S. Carlotti, F. Maggi, L. Galfetti, Vortex Combustion in a Lab-Scale Hybrid Rocket Motor, in: 52nd AIAA/SAE/ASEE Joint Propulsion Conference, American Institute of Aeronautics and Astronautics, 2016. https://doi.org/10.2514/6.2016-4562.

14) C. Paravan, R. Bisin, F. Lisi, L. Galfetti, P. Massimo, Burning Behavior Investigation of a Vortex Flow Pancake Hybrid Rocket Engine, in: AIAA Propulsion and Energy 2019 Forum, American Institute of Aeronautics and Astronautics, 2019. https://doi.org/10.2514/6.2019-4418.

15) C. Paravan, L. Galfetti, R. Bisin, F. Piscaglia, Combustion Processes in Hybrid Rockets, Int. J. Energ. Mater. Chem. Prop. 18 (2019). https://doi.org/10.1615/IntJEnergeticMaterialsChemProp.2019027834.

16) A. Hashish, C. Paravan, A. Verga, Liquefying Fuel Combustion in a Lab-scale Vortex Flow Pancake Hybrid Rocket Engine, in: AIAA Propulsion and Energy 2021 Forum, American Institute of Aeronautics and Astronautics, 2021. https://doi.org/10.2514/6.2021-3519.

17) Y. Zheng, 3 - Fabrication on bioinspired surfaces, in: Y. Zheng (Ed.), Bioinspired Design of Materials Surfaces, Elsevier, 2019: pp. 99–146. https://doi.org/10.1016/B978-0-12-814843-3.00003-X.

18) A. Schoen H., Infinite periodic minimal surfaces without self-intersections, NASA, 1970. https://ntrs.nasa.gov/citations/19700020472 (accessed December 6, 2021).

19) International Organization for Standardization, ISO 604:2002 Plastics - determination of compressive properties, 2012. https://www.iso.org/cms/render/live/en/sites/isoorg/contents/data/standard/03/12/31261.html (accessed December 7, 2021).